

Single-Molecule Microscopy Using Tunable Nanoscale Confinement

Christopher M.J. McFaul, Jason Leith, Bojing Jia, François Michaud, Adriel Arsenault,
Andrew Martin, Daniel Berard, Sabrina Leslie

McGill University, 3600 Rue University, Montreal, Canada.

ABSTRACT

We present the design, construction and implementation of a modular microscopy device that transforms a basic inverted fluorescence microscope into a versatile single-molecule imaging system. The device uses Convex Lens-Induced Confinement (CLIC)¹ to improve background rejection and extend diffusion-limited observation time. To facilitate its integration into a wide range of laboratories, this implementation of the CLIC device can use a standard flow-cell, into which the sample is loaded. By mechanically deforming the flow-cell, the device creates a tunable, wedge-shaped imaging chamber which we have modeled using finite element analysis simulations and characterized experimentally using interferometry. A powerful feature of CLIC imaging technology is the ability to examine single molecules under a continuum of applied confinement, from the nanometer to the micrometer scale. We demonstrate, using freely diffusing λ -phage DNA, that when the imposed confinement is on the scale of individual molecules their molecular conformations and diffusivity are altered significantly. To improve the flow-cell stiffness, seal, and re-usability, we have innovated the fabrication of thin PDMS-bonded flow-cells. The presented flow-cell CLIC technology can be combined with surface-lithography to provide an accessible and powerful approach to tune, trap, and image individual molecules under an extended range of imaging conditions. It is well-suited to tackling open problems in biophysics, biotechnology, nanotechnology, materials science, and chemistry.

Keywords: fluorescence microscopy, single-molecule imaging, biophysics, confinement physics, nanoscience, materials science, surface science

1. INTRODUCTION

Single-molecule fluorescence microscopy is a powerful technique which has yielded new insights into the microscopic rules governing a wide range of biological and physical systems. The ability to selectively label and optically interrogate individual molecules has enabled new biophysical measurements of the dynamics, kinetics, and mechanics governing interacting systems in biology,^{2–5} materials science,^{6, 7} chemistry,^{8, 9} and medicine.^{7, 10}

Two commonly used single-molecule techniques are confocal and total internal reflection fluorescence (TIRF) microscopy. While these techniques are used in a vast array of laboratories to understand important biological systems, they are nevertheless constrained in probing systems of interest under physiological conditions. For example, single-molecule resolution is limited to reagent concentrations less than 10 nM for confocal, and 100 nM for TIRF microscopy, corresponding to one molecule per detection volume.¹ Further, a freely diffusing protein (characterized by a diffusion coefficient of $D \sim 100 \mu\text{m}^2\text{s}^{-1}$) will exit the detection volume in hundreds of microseconds to milliseconds, for TIRF and confocal microscopy respectively.¹ These constraints on accessible reagent concentrations and observation times limit the capacity of these approaches in probing the slow dynamics or weak, cooperative, and transient interactions which characterize many physiological processes of interest.¹

A compelling challenge for modern microscopy is visualizing the trajectories of protein molecules undergoing extended molecular searches on topologically complex DNA under physiological conditions.^{11, 12} For instance, it has been theorized that a DNA repair protein's search for a lesion in the genome can be accelerated by "facilitated diffusion" which involves alternating rounds of one-dimensional and three-dimensional diffusion. Experimental investigation of these process is challenging for a number of reasons: 1.) the time for molecules to associate with one another can range from seconds to minutes; 2.) a wide field of view is necessary to visualize the

Corresponding authour: sabrina.leslie@mcgill.ca

extended search; 3.) the background fluorescence due to physiological concentrations of freely-diffusing proteins can obscure single proteins from view; and 4.) DNA topology is an important variable in these theories but is highly complex in physiological systems. The physiological significance of results obtained using confocal and TIRF microscopy can be limited by their observation conditions. For example, TIRF microscopy is typically performed using low protein concentrations and linear surface-immobilized DNA under applied flow.¹¹ While these conditions facilitate observations of molecular trajectories, they restrict the DNA topology and reagent conditions, with a number of possible consequences. For example, the rate of intersegmental transfer of protein molecules between binding sites that are proximate spatially, but distant along the contour of DNA, depends on a linear vs. complex topology. Further, cooperative interactions are not well probed at low concentrations.^{3,13}

More general approaches than surface immobilization have been made to address the difficulties faced by confocal and TIRF microscopy; however, all are subject to certain drawbacks. Zero-mode waveguides, for example, limits the excitation field to sub-micron sized chambers.¹⁴ While this approach succeeds in probing reagent concentrations up to 50 μM , its widespread adoption is limited by the need for elaborate fabrication facilities and surface-treatment protocols.¹⁵ Another attempt to image biological samples at micromolar reagent concentrations uses vesicles to encapsulate molecules;^{16,17} however, this technique suffers the disadvantage of being incompatible with extended molecules such as actin filaments.

Overcoming the simultaneous challenges of observing concentrated solutions for long time-periods is relevant not only to making advances in biophysics, but also to addressing open questions in soft-matter physics, chemistry, and nanoscience. For instance, to elucidate the microscopic rules governing the self-assembly of materials and the emergent phenomenon of active matter,¹⁸ it is essential to perform new kinds of measurements of the interactions and dynamics of individual components (e.g. microtubules, actin monomers and filaments) in free-solution, posing a challenge to current technologies.

1.1 Convex Lens-Induced Confinement (CLIC) Microscopy

With the aim of overcoming the limitations of current microscopy technologies and ultimately enabling new kinds of experiments, we have developed an accessible mechanical device which dramatically improves the imaging capabilities of a standard inverted fluorescence microscope. This device enables single-molecule imaging of fluorescent molecules at micromolar concentrations and seconds-long time periods using a microscopy principle called Convex Lens-Induced Confinement (CLIC).¹ CLIC imaging is based on a simple principle: it confines molecules within a wedge-shaped sample chamber. Reducing the detection volume suppresses background fluorescence and constrains molecules to a single focal plane, dramatically improving single-molecule imaging. Molecules confined in chamber are free to diffuse within the focal plane, e.g. allowing small proteins to be tracked for tens of seconds within a $100 \times 100 \mu\text{m}^2$ field of view. The profile of graduated confinement imposed by the CLIC imaging chamber typically varies by tens of nanometers in height over hundreds of micrometers across the field of view. This gradual change in applied confinement allows observations of molecules to be performed as a function of confinement, simply by translating the microscope objective, serving as an accessible platform for confinement physics and nanoscience research.¹

The initial implementation of CLIC imaging formed the chamber geometry by bringing the curved surface of an optical lens into direct contact with a coverslip, on which the sample was placed.¹ While this implementation dramatically improved single-molecule imaging, it had several drawbacks, including: exposing the sample to ambient conditions, allowing for sample evaporation, requiring lens-cleaning between experiments, and preventing efficient sample-exchange.

2. FLOW-CELL CLIC MICROSCOPY

In this work, we present a flow-cell implementation of CLIC imaging. The method of chamber formation is similar; a curved optical lens (which we term the “push-lens”) makes contact with the top coverslip of a flow-cell. In this case it is the deformation of the coverslip which creates the graduated chamber geometry, rather than the lens itself, offering several advantages.¹⁵ The push-lens does not make direct contact with the sample, therefore rigorous laborious cleaning protocols between measurements can be relaxed. The flow-cell geometry facilitates serial sample-replacement, reduces sample-evaporation, and requires a reduced sample volume ($\sim 8\mu\text{L}$). The

flow-cell setup can consist entirely of disposable parts and make use of existing surface-passivation and sample-preparation protocols, familiar to wide range of laboratories.

2.1 Conception of the Flow-Cell CLIC Device

Figure 1 delineates the flow-cell CLIC device presented in this work. It rests atop a sample plate, which bolts to the microscope stage. Aluminum custom fittings hold a steel shaft which acts as a rotation-axis for an extended lever arm. On this cantilever, the push-lens (Thorlabs LA4966) is fixed in a recess by means of set screws. The lever is initially raised to allow for sample insertion and lowered by adjusting the lock-nut on a finely threaded rod (Thorlabs F25US200) at the opposite end of the lever. As the lock-nut is tightened towards the plate, the lens presses down on the flow-cell, which is held over the imaging aperture by custom spring clips. A spring (Small Parts CSXX-0160-05) applies a restoring force which assures that the lens is lowered with the appropriate force to deform the coverslip (~1 N).

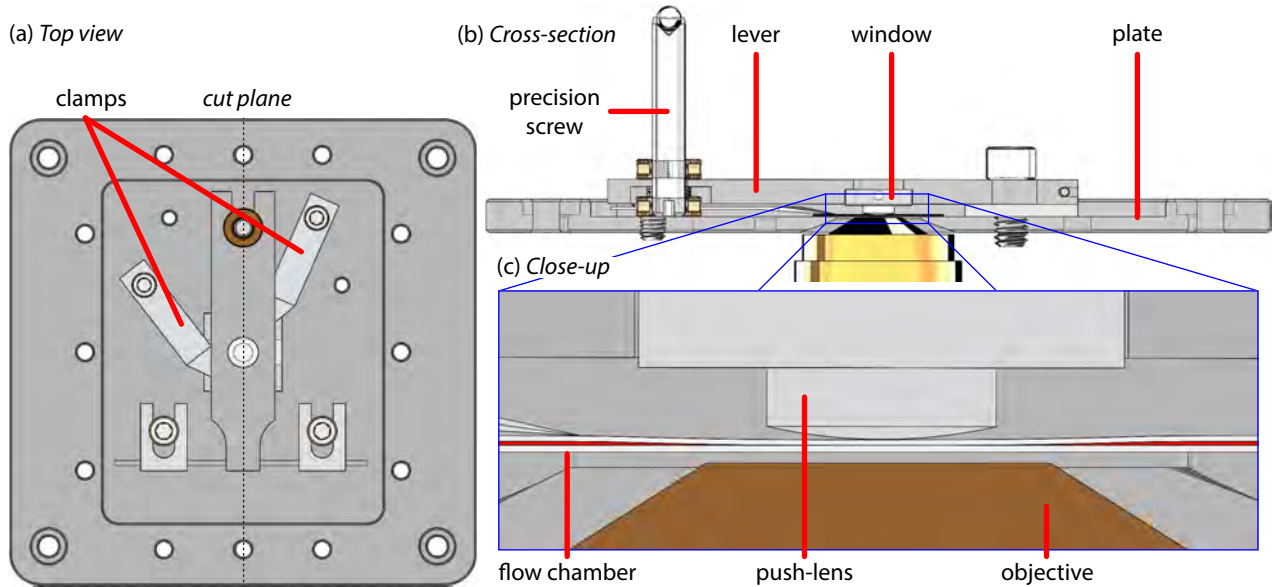


Figure 1. 3D model of the manual CLIC device. (a) Top view of the device. The four largest holes are for fastening the plate onto the microscope. The clamps can be positioned on either set of holes in the central part of the plate depending on the flow-cell size. (b) Cross-section of the CLIC device. The lever can be displaced by turning the lock-nut, which rotates on a 1/4-100" threaded screw. (c) Close-up of the cross-section at the contact point between the flow-cell and the push-lens. Here, the thickness of the tape was exaggerated (to 100 μm) to show the deformation of the top coverslip. The displayed top and bottom coverslips are respectively 145 μm and 175 μm thick. The oil objective (Nikon Apo TIRF 100x) is typically positioned 170 μm away from the bottom of the bottom coverslip.

Flow-cells were constructed using two planar coverslips, sealed together using either double-sided adhesive or bonded PDMS films. Figure 3 shows rectangular and circular flow-channels, which can be cut using either a razor blade or laser-ablation (PBS Engraving Inc., Ontario, Canada). Many laboratories construct standard rectangular flow-cells using drugstore-available double-sided adhesive (Scotch Double Stick Tape, 3M Inc., ~ 100 μm thick). In contrast, flow-cell CLIC microscopy benefits from a reduced channel height (e.g. using 10, 30, 50 μm -thick adhesive provided by Nitto Denko 5301, 5303, 5305 respectively, or custom PDMS films) as this reduces the final applied confinement gradient.

2.2 Development of PDMS-bonded flow-cells

The reliability and reproducibility of a given flow-cell can be improved by increasing the spatial homogeneity and bond strength of the adhesive-coverslip interface, as well as the stiffness of the adhesive walls. To meet these aims, we present a soft lithography protocol and a suite of devices to create thin polydimethylsiloxane (PDMS) films. Using these films yielded additional benefits, including reducing the flow-cell swelling and relaxation time after compressing the chamber, in comparison to the double-sided adhesive, and also allowing for fine-tuning of the film thickness and stiffness by adjusting the spin coating settings and elastomer-to-crosslinking-polymer ratio.

The PDMS films presented in this work were fabricated using a 5:1 ratio of PDMS elastomer and cross-linking agent (Sylgard 184, Dow Corning, Midland, MI). The wafers were passivated using trichloro(1,1,2,2-perfluorocetyl)silane (Sigma Aldrich, Milwaukee, WI) for 90 minutes in a vacuum dessicator prior to spin-coating. For a final film thickness of 30 μm , a drop of PDMS was applied to the wafer, spun at 2800 rpm for 35 seconds, and cured at 60 °C overnight. For a final thickness of 50 μm , a drop of PDMS was spun at 1800 rpm for 35 seconds, and cured at 60 °C overnight. Curing the film for 48 additional hours stiffened the PDMS film and facilitated its removal from the wafer without breakage.

A key challenge to this work was holding and cutting delicate, micron-thin PDMS films without inducing damage or wrinkles. The solution to this problem involved using a transfer ring, using methods described by Samuel et al. as a starting point (Fig. 2a).¹⁹ To prepare the ring, liquid PDMS was inserted into an annular aluminum mold and baked overnight at 60 °C. The surfaces of the transfer ring and the PDMS film were oxidized by oxygen-plasma (PlasmaPreen) for one minute, and the transfer ring was bonded to the perimeter of the film atop the wafer. By gently lifting the transfer ring, the PDMS film peeled off the wafer, held flat by surface tension (Fig. 2b). Prior to cutting the flow-channel pattern, the PDMS film was transferred to a Petri dish. An aluminum stencil was placed on top of the film (Fig. 2c). The pattern was cut by tracing a razor blade along the circumference of the stencil. Unwanted PDMS was subsequently removed with tweezers.

Flow-cells were formed using 25 mm x 25 mm No. 1 and 1.5 Goldseal (Ted Pella, Redding, CA) top and bottom coverslips, respectively. Loading holes were sandblasted into the corners of top coverslips prior to cleaning, in the case of circular flow channels. Following

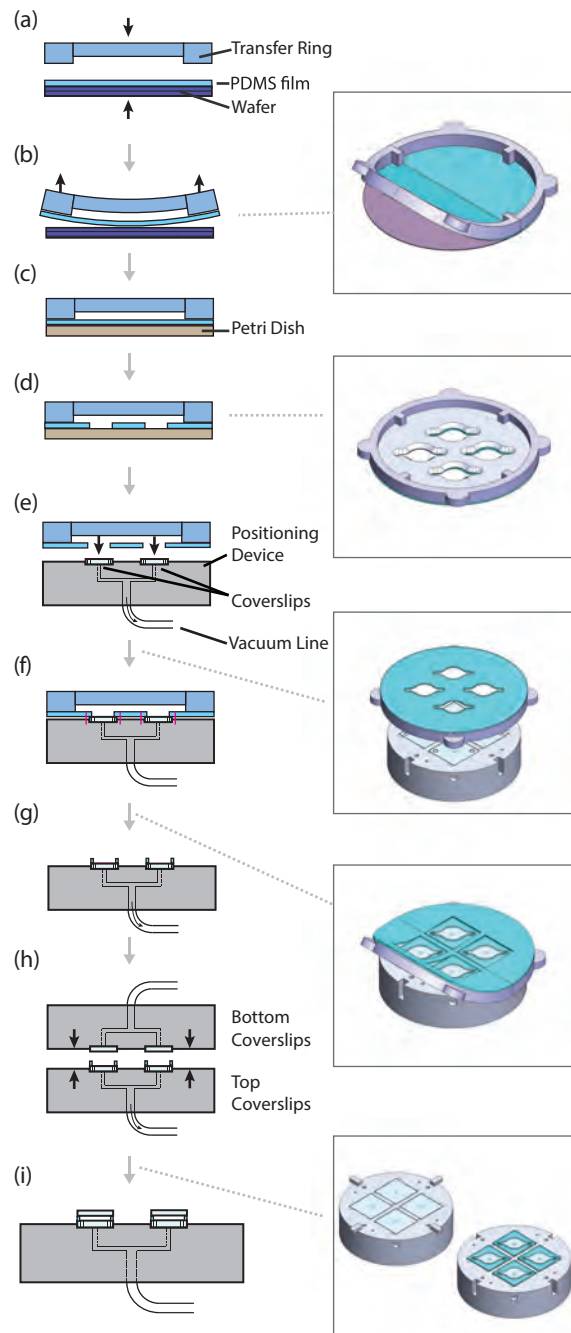


Figure 2. Schematic of PDMS flow-cell assembly. See text for step-by-step description.

the coverslip cleaning (using a “piranha” solution of 2:1 sulfuric acid to 30% hydrogen peroxide, for 45 minutes), the top coverslip and the patterned PDMS film were plasma-activated for 30 seconds, respectively. The top coverslip was placed in a custom positioning array with shallow grooves, held in place by vacuum-suction (Fig. 2e). The PDMS patterns were aligned with respect to the sample-loading holes in the top coverslip, and the PDMS film was brought into contact for bonding. Excess PDMS was trimmed around the edges of the coverslip using a razor blade after bonding. Once the transfer ring was lifted (Fig. 2f), the PDMS-embossed top coverslips (Fig. 2g) and bottom coverslips were plasma-activated for 30 seconds. Subsequently, the top and bottom coverslips, held within the grooves of opposing positioning-arrays, were gently brought in contact (Fig. 2h). The vacuum was released and the completed flow-cells were removed for storage and use (Fig. 2i).

3. QUANTITATIVE SIMULATIONS OF THE FLOW-CELL CLIC GEOMETRY

We have developed a predictive model for the CLIC chamber geometry in order to equip researchers with quantitative measures of key microscopy parameters as a function of readily-available instrument components. In order to apply flow-cell CLIC microscopy to new kinds of experiments in a wide range of disciplines (e.g. biophysics, nanoscience, surface chemistry, and materials science), a quantitative understanding of the imaging chamber geometry is important.

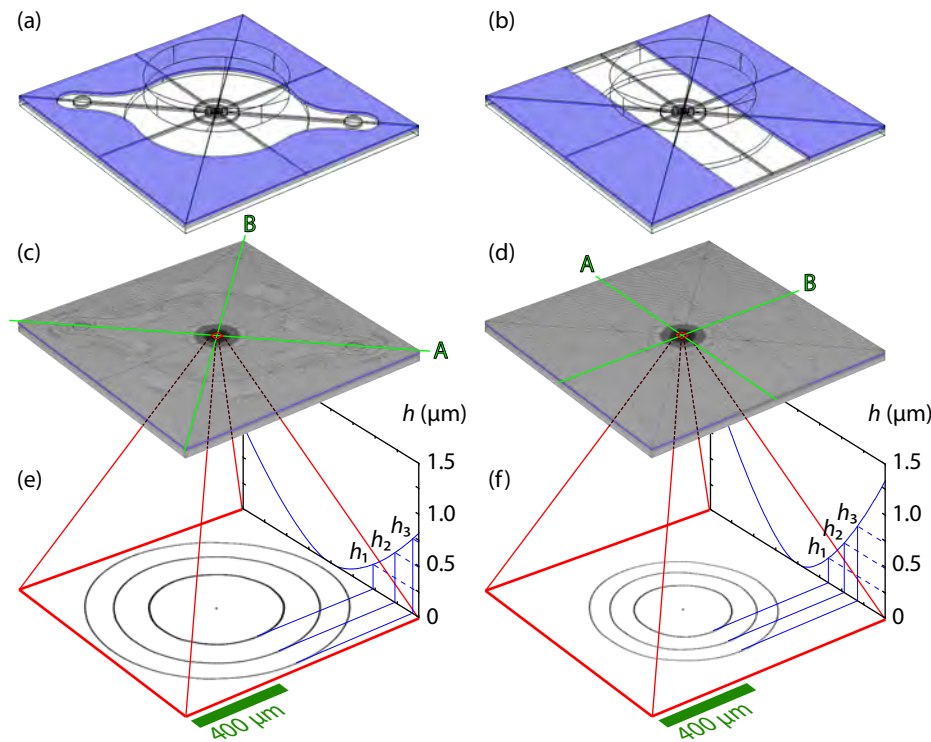


Figure 3. Model used in simulations. (a, b) Wireframe renderings of the circular and rectangular flow-cells, showing the push-lens above and plate below. The 30- μm thick PDMS film is highlighted in blue. (c) Overview of the mesh used for the circular flow-cell and the plate. The mesh element precision is refined toward the center, where it is 23 μm . (d) Similar overview of the mesh used for the rectangular flow-cell and the plate, with minimum mesh element size at the center of 20 μm . (e) Chamber height profile of compressed circular flow-channel (side projection) and height contours corresponding to dark interferometry fringes (bottom projection). (f) Chamber height profile of compressed rectangular flow-channel (side projection) and height contours corresponding to dark interferometry fringes (bottom projection).

Using COMSOL Multiphysics (version 4.3b) we have simulated the CLIC imaging chamber implemented using two kinds of PDMS flow-cells: one with a circular channel with inlets (Fig.3a) and one with an 8-mm wide rectangular channel (Fig.3b). We have modeled the chamber geometry as a function of accessible parameters,

including the film thickness, radius of curvature of the push-lens (R_p), and *over-push* distance, defined as the distance by which the push-lens is translated past coverslip-coverslip contact. This predictive model enables experiment-specific understanding and selection of important chamber parameters such as the size of the in-focus region and radius of curvature of the chamber. Throughout this section, default device parameters are taken as: 30- μm thick film, a 145- μm thick top coverslip (#1 coverslip), a 175- μm thick bottom coverslip (#1.5 coverslip), a 30-mm focal length push-lens (Thorlabs LA4966), and zero over-push distance. An applied over-push causes the top coverslip to indent the bottom coverslip in a circular region of mean radius of contact r_b , as illustrated by Fig. 4.

In the simplest imaging setup, the objective is translated in a single horizontal plane containing the contact point (e.g. without using an auto-focus feedback mechanism). In the final CLIC imaging chamber, the bottom surface of the bottom coverslip curves away from the objective, by an amount equal to δ . Its top surface curves by the same amount, as illustrated by Fig. 4b. Molecules appear in-focus when the separation between the plane containing the contact point and top confining surface, $h + \delta$, is less than the focal depth, taken to be 1.5 μm . Tables 1 and 2 show the size of this in-focus region. The size of this region increases when the tape thickness decreases, and is weakly affected by the over-push distance.

For the circular flow cell, the flexure of the bottom coverslip towards the objective is effectively negligible for typical operating parameters. The in-focus region is characterized by a diameter of 1506 μm on major axis A and 1477 μm on minor axis B, and maximum chamber height of 1.46 μm on major axis A and 1.45 μm on minor axis B (see Fig. 3 c,d). This region can be extended to 1528 μm on major axis A and 1509 μm on minor axis B, corresponding to a chamber height equal to the focal depth, by employing an auto-focus mechanism. Similarly, for the rectangular flow-cell, the in-focus region is characterized by a diameter of 1068 μm on major axis A (988 μm on minor axis B), and a maximum chamber height of 1.33 μm on major axis A (1.41 μm on minor axis B). This region can be extended to 1130 μm on major axis and 1016 μm on minor axis by using an auto-focus mechanism.

We define the imaging chamber radius of curvature, R_c , by fitting the chamber height profile to

$$h = r^2/(2R_c), \quad (1)$$

where h is the separation between the chamber walls and r is the radial distance from the contact point (Fig. 3c). The circular chamber model is approximately radially symmetric, with percentage difference between its radii of curvature along axes A and B of 1% (Fig.3 c, d). In contrast, the rectangular chamber is elliptical, with radius of curvature along axis A 14% larger than along axis B. The pressure applied by the clips on the flow-cell are not found to influence the shape of the chamber inside a 300 μm radius; the clips were assumed to be positioned along symmetry axes B in both models.

R_c decreases significantly as a function of increasing tape thickness and increases slightly as a function of over-pushing distance, as shown by Tables 1 (right section) and 2 (right section). The accessible range of radii of curvature (as large as 424 mm for a circular and 230 mm for a rectangular chamber) greatly exceed values accessible to lens-coverslip CLIC (a practical upper-limit for small-size commercial lenses is $R = 46$ mm for Thorlabs LA4600).

The ability to create imaging chambers characterized by larger radii of curvature, and hence lower applied confinement gradients, is useful for a number of applications: spectroscopy of small molecules (e.g. potential

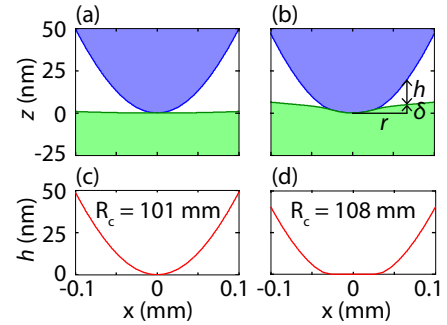


Figure 4. Schematic of the coverslip-coverslip contact point along the designated minor axis for the simulated circular chamber flow-cell. (a) Contact between the top (blue) and bottom (green) coverslips for over-push = 0 μm . The bottom coverslip is slightly deformed. (b) Contact between the cover slips for over-push = 1 μm . The quantities δ and h , as defined in the text, are shown as functions of the radius from the contact point r (c) Chamber height profile for over-push = 0 μm with radius of curvature computed from a quadratic fit performed inside the displayed region. (d) Chamber height profile for over-push = 1 μm . The chamber is flat inside a region of contact with radius of curvature $r_b = 39 \mu\text{m}$ computed similarly.

measurements of protein-folding as a function of applied confinement), resolving size distributions of small molecules,¹ and potentially using CLIC as a tunable lid for sealing coverslip-embedded features.

3.1 Model Geometry and Mesh

The simulation models were comprised of a spherical fused silica plano-convex push-lens (Thorlabs LA4966), two parallel glass coverslips coupled by a PDMS film (Young's modulus of 1.96 MPa) and a rigid sample plate with a central hole (8.1-mm radius). For computational simplicity, the models did not include the sample fluid between the two coverslips which is free to exit the outlet during compression.

The model-meshes (Fig. 3 c,d) were fine-tuned to ensure convergence of results. The push-lens was modeled using a tetrahedral mesh, which was progressively more precise towards the center. The average element edge size was reduced from 216 μm to 4 μm near the contact point. The coverslips were modeled using a triangular surface mesh, which was swept through the bottom in equally spaced layers. The meshes included two layers on the top coverslip and three on the bottom coverslip. For the circular [rectangular] chamber model, the size of the average triangle-edge starts from 148 μm [138 μm] in the tape and chamber region, and decreases progressively from 103 μm to 23 μm [88 μm to 20 μm] within the three concentric circles shown, characterized by radii of 2 mm, 1 mm and 0.5 mm. The mesh for the film was identical to the corresponding regions in the coverslips; the holder was also constructed using a tetrahedral mesh. The deformed chamber geometry, even close to the center, was shown to depend heavily on the resolution of the mesh outside the central precision circles. For each chamber geometry and film thickness, multiple simulations were performed with increasing mesh resolution until a convergent value for R_c was determined, presented in Tables 1 and 2.

$h_{\text{PDMS}}(\mu\text{m})$	push = 0 μm			1 μm		10 μm	
	R_c	R_c	r_b	R_c	R_c	r_b	r_b
10	424 [418]	440 [433]	62 [61]	454 [446]	454 [446]	106 [105]	106 [105]
30	149 [147]	153 [151]	39 [39]	157 [155]	157 [155]	70 [69]	70 [69]
50	92 [91]	94 [92]	29 [29]	96 [95]	96 [95]	62 [61]	62 [61]

Table 1. Circular flow-cell data for different film thicknesses h_{PDMS} . (Left) Radius of the region of focus (μm) along axis A [B]. (Right) Radius of curvature of the chamber R_c (mm) and region of contact r_b (μm) along axis A [B].

$h_{\text{PDMS}}(\mu\text{m})$	push = 0 μm			1 μm		10 μm	
	R_c	R_c	r_b	R_c	R_c	r_b	r_b
10	230 [201]	238 [207]	47 [45]	250 [214]	250 [214]	87 [83]	87 [83]
30	84 [74]	86 [75]	28 [26]	88 [77]	88 [77]	61 [59]	61 [59]
50	53 [46]	53 [47]	22 [22]	54 [48]	54 [48]	46 [44]	46 [44]

Table 2. Rectangular flow-cell data for different thicknesses h_{PDMS} . (Left) Radius of the region of focus (μm) along axis A [B]. (Right) Radius of curvature of the chamber R_c (mm) and region of contact r_b (μm) along axis A [B].

4. CHAMBER CHARACTERIZATION

To characterize the imaging chamber geometries formed using circular and rectangular PDMS flow-cells, two kinds of measurements were acquired. 1.) Microscopy of the chamber height profile was performed using a.) direct interferometry and b.) fluorescence imaging of an in-situ fluorophore. 2.) The thicknesses of the uncomressed PDMS flow-cells were measured in-situ using the point spread function (PSF) of surface-adhered fluorescent beads.

Figure 5 displays an array of high-resolution images acquired over an $880 \times 880 \mu\text{m}^2$ region by raster-scanning the microscope stage (PI M-545 Open-Frame Microscope Stage) relative to the objective (Nikon Apo TIRF 100 \times). When measuring the chamber geometry using interferometry, the chamber was illuminated using a 488-nm Coherent Sapphire laser and a pattern of *Newton's rings* was observed (Fig 5). The resulting interference minima were spaced by $\lambda/2n \approx 183.4 \text{ nm}$, which provided quantitative contours of the chamber height profile. Here, $\lambda = 488 \text{ nm}$ and $n = 1.33$ corresponds to the excitation wavelength and refractive index of the sample. Additionally, Fig. 5 c,d depict fluorescence images of a fluorophore (AlexaFluor 647), illuminated using a Coherent OBIS 647 laser. Since the Alexa fluorophore has a diameter of $\sim 1 \text{ nm}$, the dye concentration is

constant (for heights $\simeq 3$ nm). Consequently, the observed fluorescent intensity is proportional to chamber height.

A fourth-order polynomial was fit to the dye fluorescence intensity to obtain a function proportional to the local chamber height. Once normalized and offset-corrected, this fit-function was scaled to represent the chamber height, e.g. by taking the height at the m^{th} interference minima to be $h = \frac{m\lambda}{2n}$ and the height at contact to be ~ 2 nm, corresponding to the average expected surface-roughness.

To quantify the chamber radius of curvature, R_c , and directly compare the measured and modeled chamber geometries, cross sections of both height functions were taken along the major and minor axes (averaged over $1.6 \mu\text{m}$ in the transverse direction). These cross-sections were fit to a quadratic function (Eq. 1) to extract representative values of R_c , which were used to compare the measured and simulated chamber geometries.

Three kinds of PDMS flow-cell geometries (circular, thin rectangular and thick rectangular) were prepared and used for flow-cell CLIC microscopy experiments. To test for variability in flow-cell construction, each geometry was implemented in three PDMS flow-cells. To test for variability in the imaging-chamber formation, three CLIC experiments were performed using equilibrated, fully compressed chambers. Figure 5a demonstrates a representative circular chamber (formed using $54.4 \pm 0.4 \mu\text{m}$ thick PDMS), which was characterized by a major radius of curvature of $196 \pm 16 \text{ mm}$ and a minor radius of curvature of $162 \pm 2 \text{ mm}$. Figure 5b demonstrates a representative “thin” rectangular chamber (formed using $35.6 \pm 0.5 \mu\text{m}$ thick PDMS), which was characterized by a major radius of curvature of $99 \pm 3 \text{ mm}$ and a minor radius of curvature of $88 \pm 3 \text{ mm}$. A representative “thick” rectangular chamber (formed using $46.5 \pm 0.4 \mu\text{m}$ thick PDMS) was characterized by a major radius of curvature of $58 \pm 3 \text{ mm}$, a minor radius of curvature of $47 \pm 3 \text{ mm}$. The measured R_c values are in good agreement with the model-predicted values. The thick rectangular chamber, with an uncompressed height of approximately $46 \mu\text{m}$, is predicted to be characterized by a major $R_c = 54 \text{ mm}$ and minor $R_c = 48 \text{ mm}$, using the default parameters described in Sec. 3.

The height of the uncompressed chamber (corresponding to the PDMS thickness) was measured using the point spread function (PSF) of sub-diffraction-sized fluorescent beads (Thermo Scientific Fluoro-Max G200, 3.96 pM concentration) adhered to the top and bottom chamber surfaces. The beads were inserted into the chamber and surface-immobilized using a 10% poly-L-lysine solution, subsequent to the flow-cell CLIC microscopy experiments. A series of images were acquired while the objective was translated vertically through the chamber in increments of 100 nm . The PSF of surface-adhered beads was determined by fitting two-dimensional Gaussians

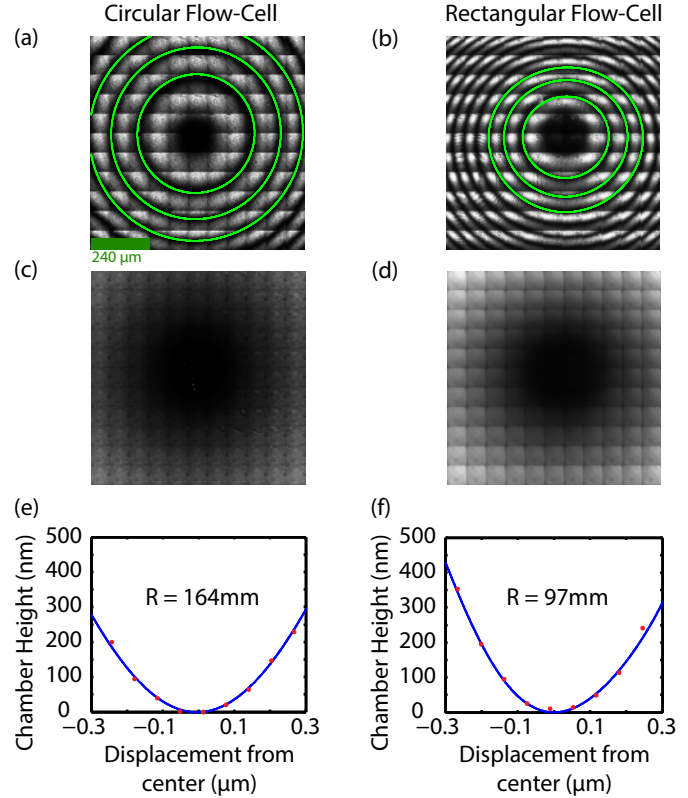


Figure 5. PDMS-bonded flow-cell CLIC imaging chambers, shown using identical distance-scales. (a, b) Interferometry of the chamber height profile, with overlaid height contours (green) corresponding to integer multiples of $\frac{\lambda}{2n}$ where $\lambda = 488 \text{ nm}$ and $n = 1.33$. (c, d) Fluorescence images of Alexa647 dye shown on the same contrast scale. (e, f) Cross sections of dye fluorescence intensity, taken along the major R_c axis (red dots) and the described polynomial fit (blue line).

to each image. The PDMS thickness was determined by calculating the difference in objective heights between the two PSF minima, corresponding to in-focus beads immobilized on each surface.

5. IMAGING FREELY DIFFUSING DNA UNDER CONFINEMENT

Figure 6a,b present fluorescent images of freely diffusing λ -phage DNA, stained with YOYO-1 fluorescent dye. The chamber heights for the molecules shown and analyzed lie between 460–640 nm and 1100–1470 nm, respectively. The latter is approximately the bulk radius of gyration, R_g , which we estimate at our very low ionic strength of 1.35 mM to be $1.1 \pm 0.1 \mu\text{m}$ (see Methods), and the former is much smaller. Polymer chains generally²⁰ and DNA in particular²¹ have been shown to experience the effects of confinement at heights $\lesssim 2R_g$, so for both ranges of chamber heights our molecules are confined, with stronger confinement effects at the smaller chamber height.

The corresponding trajectory analysis and the distribution of diffusion coefficients, D , shown in Fig. 6c,d, demonstrate the effect of the imposed confinement in slowing the DNA diffusion. Similarly, Fig. 6 e,f demonstrate an increase in the in-plane radius of gyration, $R_{||}$ with greater confinement. The molecules were tracked for a total of 55 s (1000 frames). Figure 6c,d are based on 66 and 92 lifetime-weighted particles, respectively.

According to deGennes's blob theory,²² polymers confined to a slit of height H such that $p < H \lesssim R_g$, where p is the persistence length, should have $D \sim H^{2/3}$ and $R_{||} \sim H^{-1/4}$. We observe diffusion coefficients of $0.184 \pm 0.019 \mu\text{m}^2/\text{s}$ and $0.230 \pm 0.024 \mu\text{m}^2/\text{s}$ for heights within the ranges of $460 \text{ nm} < H < 640 \text{ nm}$ and $1100 < H < 1470 \text{ nm}$, respectively, for a ratio of $D(550\text{nm})/D(1280\text{nm}) = 0.80 \pm 0.11$, and $R_{||}$'s of $1.20 \pm 0.22 \mu\text{m}$ and $1.08 \pm 0.14 \mu\text{m}$, for a ratio of $R_{||}(550\text{nm})/R_{||}(1280\text{nm}) = 1.11 \pm 0.03$ (see Methods). Predicted ratios for D and $R_{||}$ are 0.58 ± 0.12 and 1.24 ± 0.10 , respectively, with uncertainties dominated by the spread in chamber height (see Methods). While the measured and predicted ratios for $R_{||}$ agree within error, the blob theory's scaling for D is described by a stronger dependence on H than we observe. This discrepancy has been observed by other groups,^{23–25} and has recently been explained by Dai et al.²⁶ as resulting from a deviation in a semiflexible polymer's pair correlation function at small ($< p$) lengthscales from classical Flory scaling.

5.1 Methods

5.1.1 Cleaning and Experimental Buffer

Coverslips for all experiments were cleaned using 2:1 sulfuric acid to 30% hydrogen peroxide solution (Piranha) for 45 minutes. The coverslips were then treated with 1M potassium hydroxide for 15 minutes.

The final experimental buffer consisted of 1.445 mM Tris base, 0.445 mM boric acid, 0.1 mM EDTA, 0.32 mM HCl, 577 nM AlexaFluor 647, 285 mM 2-mercaptoethanol and 13 pM of YOYO-1 fluorescently stained λ -phage DNA at a labeling ratio of 1:10 fluorophores per base pair. This solution had a final pH of 7.1 and an ionic concentration of 1.35 mM.

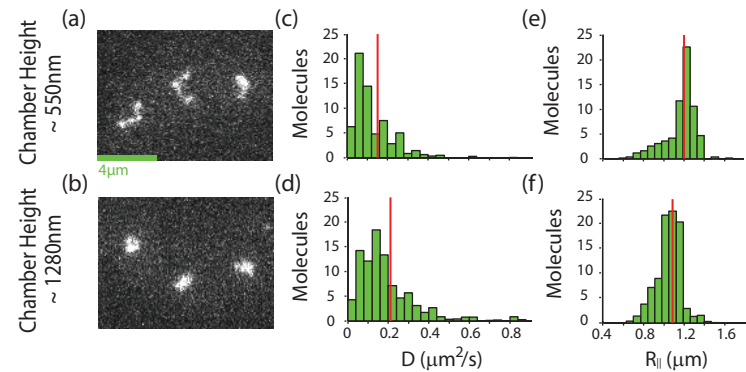


Figure 6. Diffusion coefficients and in-plane radius of gyration of λ -phage DNA. (a)(b) Images of fluorescently labeled DNA at heights of $H \approx 550\text{nm}$ and $H \approx 1280\text{nm}$, respectively. (c)(d) Histograms of diffusion coefficients, D , for freely diffusing molecules. The mean values (designated by red lines) are $0.184 \pm 0.019 \mu\text{m}^2/\text{s}$ (550 nm) and $0.230 \pm 0.024 \mu\text{m}^2/\text{s}$ (1280nm). (e)(f) Histograms of in-plane radius of gyration, $R_{||}$. Mean values are $1.20 \pm 0.22 \mu\text{m}$ (550 nm) and $1.08 \pm 0.14 \mu\text{m}$ (1280 nm).

5.1.2 Molecule Tracking and Analysis

Molecules were identified by a 4-step process. First, pixels were converted to binary values about a threshold that was chosen to eliminate anything but lambda DNA. Then a series of image-processing operations (using the Matlab command “`bwmorph`”) were used to clean up the image and identify molecules (1 quorum fill, 3 dilations, and 2 erosions). Analysis parameters were chosen so as to minimize the loss or double-identification of dim sections of elongated molecules.

Once the molecules were located in each frame, the intensity-weighted centroid for each molecule was computed using the Matlab command “`regionprops`”. Movies were manually examined for misattributed centroids owing to two particles in proximity being identified as one, or a single particle being assigned two centroids. The centroids were then linked between frames to form particle trajectories. Only trajectories longer than 2.7 s (50 frames) were included in the results presented in Fig. 6. Particle trajectories were plotted on top of their respective movies and erroneous parts of trajectories were eliminated manually.

Diffusion coefficients were calculated using the maximum likelihood estimator (MLE) of a particle’s diffusion co-efficient given its trajectory.²⁷ The in-plane radius of gyration, R_{\parallel} , is the square root of the mean squared distance from the centroid of the particle, $\bar{\mathbf{r}}$ weighted by the pixels’ intensities, I ,

$$R_{\parallel} = \sqrt{\frac{\sum_i (\mathbf{r}_i - \bar{\mathbf{r}})^2 I_i}{\sum_i I_i}}, \quad (2)$$

where the sum is over all the pixels i deemed in the image analysis to comprise the particle. The mean diffusion coefficient and mean in-plane radius of gyration for a given set of particles was weighted by the particles’ lifetimes. Uncertainty in D , R_{\parallel} , and in their respective ratios for different heights, $D(550\text{nm})/D(1280\text{nm})$ and $R_{\parallel}(550\text{nm})/R_{\parallel}(1280\text{nm})$, span a 95% confidence interval using 10,000 bootstrap re-samples.

5.1.3 Estimation of R_g

We estimate the bulk radius of gyration, R_g of YOYO-1-stained lambda DNA as follows. The contour length L of lambda DNA is 16.5 μm , but is elongated by the intercalating YOYO-1 stain. The elongation per YOYO-1 molecule has been measured to be $0.51 \pm 0.13 \text{ nm}$;²⁸ we stained our DNA with a 1:10 ratio of YOYO-1 molecules to base pairs, yielding a total length of $19.0 \pm 0.6 \text{ }\mu\text{m}$.

Based on Schaefer et al.’s modification of Flory theory,²⁹ the radius of gyration of a semi-flexible polymer in a good solvent is $(\pi p w / 4)^{1/5} L^{3/5}$, where p is the persistence length and w is the width of the polymer. Using the theory of Manning,³⁰ we estimate the persistence length of our DNA at 1.35 mM ionic strength to be $71 \pm 9 \text{ nm}$, with uncertainty based on the precision of parameters employed by Manning and the precision of pipetting ionic buffer components. Using $w = 5 \text{ nm}$ and the above values for L and p gives an estimate of the bulk R_g of $1.1 \pm 0.1 \text{ }\mu\text{m}$.

5.1.4 Chamber Geometry and Imaging Parameters

The chamber used for the λ -phage DNA experiments was constructed from a 25 mm x 25 mm No. 1 Goldseal (Ted Pella, Redding, CA) top coverslip and 25 mm x 25 mm No. 1.5 bottom coverslip (the top coverslip did not have sand-blasted inlets and outlets). A 5.5 μL volume of sample was placed on the bottom coverslip and laser cut double sided 30 μm tape (Nitto Denko No. 5603) with the same geometry as seen in Fig. 3a was used to seal the coverslips together. This geometry offered the advantage of a completely sealed chamber and eliminated evaporation. The top coverslip was pressed into contact with the bottom coverslip and an equilibration period of 45 minutes was allowed before molecule trajectories were imaged, with coverslip-coverslip contact confirmed. Data was acquired at a series of locations around the 3rd and 7th dark interference rings (as in Fig. 5a,b), corresponding to average heights of $H \approx 550 \text{ nm}$ and $H \approx 1280 \text{ nm}$ respectively.

The DNA molecules were excited with a 488-nm OPSL laser (Coherent) with emission collected by a 100 \times Apo-TIRF objective (Nikon) on a custom-built inverted microscope. Imaging was performed used a cooled EM-CCD camera (Andor iXon Ultra), 30 ms-exposure frames acquired at a rate of 18.2 Hz, and an EM gain of 300. Acquisition was performed using μ Manager³¹ driven by custom scripts.

6. CONCLUSION AND OUTLOOK

We have demonstrated the construction and operation of a powerful and accessible single-molecule microscopy device, termed flow-cell CLIC. This device extends single-molecule microscopy to a much wider range of reagent concentrations and observation timescales than standard techniques can access, and serves as a novel platform for nanoscale confinement experiments. For improved operation of this device, we have engineered a method for fabricating precision flow-cells using PDMS films. To understand and optimize the operation and geometry of this nanoscale device, we have created and tested a predictive model of the flow-cell CLIC imaging chamber geometry.

The imaging benefits delivered by flow-cell CLIC microscopy are transferrable to many fields of research. For example, CLIC imaging can be used to shed new light into the molecular underpinnings of the emergent phenomenon of *active matter*, a new area of soft-materials research.¹⁸ Single-molecule measurements of the protein-polymer and polymer-polymer interactions driving these macroscopic dynamic systems are lacking, which must be examined away from surfaces due to depletion effects, for which CLIC imaging is ideally suited.

The use of the CLIC device's ability to tune interactions between molecules through varying levels of confinement is transferrable to the fields of nanotechnology, materials science, and chemistry.³² For example, the CLIC device could potentially be used to guide the creation of plasmonic nanocrystal arrays which form through self-assembly. The self-assembly process is typically influenced by the choice of nano-crystal size, shape, surface chemistry, and properties of the surrounding polymer matrix.³³ The CLIC device would provide a convenient microscopy platform suitable for interrogating these structures under tunable applied confinement and could simplify the preparation and study of these thin films by potentially constraining crystals to a single layer. The adjustable dimensionality offered by this device, as well as its potential modification by surface-lithography, would introduce a new level of experimental control over the free energy profile governing the crystal formation.

ACKNOWLEDGMENTS

The authors would like to thank the agencies who have contributed funding for this project: CRSNG NSERC, the Canada Foundation for Innovation (Innovation.ca), and the Department of Physics, McGill University. Chris McFaul would like to thank the NSERC CREATE program, Bionano for a fellowship, and Dr. Jason Leith and Adriel Arsenault are grateful for their fellowships awarded from the Cellular Dynamics of Macromolecular Complexes Program (CDMC). We are also grateful to the μ Manager³¹ software and development team.

REFERENCES

1. Leslie, S. R., Fields, A. P., and E., C. A., "Convex lens-induced confinement for imaging single molecules," *Anal. Chem.* **82**, 6224–6229 (2010).
2. Moerner, W. E., "New directions in single-molecule imaging and analysis," *Proceedings of the National Academy of Sciences* **104**(31), 12596–12602 (2007).
3. Joo, C., Balci, H., Ishitsuka, Y., Buranachai, C., and Ha, T., "Advances in single-molecule fluorescence methods for molecular biology," *Annual Review of Biochemistry* **77**(1), 51–76 (2008).
4. Jain, A., Liu, R., Ramani, B., Arauz, E., Ishitsuka, Y., Ragunathan, K., Park, J., Chen, J., Xiang, Y. K., and Ha, T., "Probing cellular protein complexes using single-molecule pull-down," *Nature* **473**, 484–488 (2011).
5. Duzdevich, D. and Greene, E. C., "Towards physiological complexity with in vitro single-molecule biophysics," *Philosophical Transactions of the Royal Society B: Biological Sciences* **368**(1611) (2013).
6. Barbara, P. F., Gesquiere, A. J., Park, S.-J., and Lee, Y. J., "Single-molecule spectroscopy of conjugated polymers," *Accounts of Chemical Research* **38**(7), 602–610 (2005).
7. Guo, X., "Single-molecule electrical biosensors based on single-walled carbon nanotubes," *Advanced Materials* **25**(25), 3397–3408 (2013).
8. Kulzer, F. and Orrit, M., "Single-molecule optics," *Annual Review of Physical Chemistry* **55**(1), 585–611 (2004).
9. Lee, T., Gonzalez, J., Zheng, J., and Dickson, R., "Single-molecule optoelectronics," *Acc Chem Res* **38**(7), 534–41 (2005).

10. Navin, N. and Hicks, J., "Future medical applications of single-cell sequencing in cancer," *Genome Medicine* **3**(5), 31 (2011).
11. Gorman, J. and Greene, E. C., "Visualizing one-dimensional diffusion of proteins along DNA," *Nature Structural & Molecular Biology* **15**(8), 768–774 (2008).
12. Gibb, B., Silverstein, T. D., Finkelstein, I. J., and Greene, E. C., "Single-stranded dna curtains for real-time single-molecule visualization of protein-DNA interactions," *Analytical Chemistry* **84**(18), 7607–7612 (2012).
13. Cohen, A., Fields, A., Hou, J., Leslie, S., and Shon, M., "In Honor of W.E. Moerner: Confining Molecules for Single-Molecule Spectroscopy," *Israel Journal of Chemistry* **49**(3-4), 275–282 (2009).
14. Levene, M. J., Korlach, J., Turner, S. W., Foquet, M., Craighead, H. G., and Webb, W. W., "Zero-mode waveguides for single-molecule analysis at high concentrations," *Science* **299**(5607), 682–6 (2003).
15. Elting, M. and Leslie, S., "Single-molecule fluorescence imaging of processive myosin with enhanced background suppression using linear zero-mode waveguides (ZMWs) and convex," *Optics Express* **21**(1), 1189–1202 (2013).
16. Chiu, D. T., Lorenz, R. M., and Jeffries, G. D. M., "Droplets for ultrasmall-volume analysis," *Analytical chemistry* **81**(13), 5111–8 (2009).
17. Boukobza, E., Sonnenfeld, A., and Haran, G., "Immobilization in Surface-Tethered Lipid Vesicles as a New Tool for Single Biomolecule Spectroscopy," *The Journal of Physical Chemistry B* **105**(48), 12165–12170 (2001).
18. Sanchez, T., Chen, D. T. N., DeCamp, S. J., Heymann, M., and Dogic, Z., "Spontaneous motion in hierarchically assembled active matter," *Nature* **491**(7424), 431–4 (2012).
19. Samuel, R., Jayant Sant, H., Jao, F., Johnson, C. R., and K., G. B., "Fabrication of a mri standardization device from stacking highly patterned thin pdms layers," in [*Proc. of AIChE 2010, Salt Lake City, Utah, November 7-12 2010*], 744a (2010).
20. C.E. Cordeiro, M. Molisana, and D. Thirumalai, "Shape of confined polymer chains," *J. Phys. II France* **7**(3), 433–447 (1997).
21. Tang, J., Levy, S. L., Trahan, D. W., Jones, J. J., Craighead, H. G., and Doyle, P. S., "Revisiting the conformation and dynamics of dna in slitlike confinement," *Macromolecules* **43**, 7368–7377 (2010).
22. de Gennes, P., [*Scaling concepts in polymer physics*], Cornell University Press (1979).
23. Balducci, A., Mao, P., Han, J., and Doyle, P. S., "Double-stranded dna diffusion in slitlike nanochannels," *Macromolecules* **39**(18), 6273–6281 (2006).
24. Dai, L., Jones, J. J., van der Maarel, J. R. C., and Doyle, P. S., "A systematic study of dna conformation in slitlike confinement," *Soft Matter* **8**, 2972–2982 (2012).
25. Strychalski, E. A., Levy, S. L., and Craighead, H. G., "Diffusion of dna in nanoslits," *Macromolecules* **41**(20), 7716–7721 (2008).
26. Dai, L., Tree, D. R., van der Maarel, J. R. C., Dorfman, K. D., and Doyle, P. S., "Revisiting blob theory for dna diffusivity in slitlike confinement," *Phys. Rev. Lett.* **110**, 168105 (2013).
27. Leith, J. S., Tafvizi, A., Huang, F., Uspal, W. E., Doyle, P. S., Fersht, A. R., Mirny, L. A., and van Oijen, A. M., "Sequence-dependent sliding kinetics of p53," *Proceedings of the National Academy of Sciences* **109**(41), 16552–16557 (2012).
28. Günther, K., Mertig, M., and Seidel, R., "Mechanical and structural properties of yoyo-1 complexed dna," *Nucleic Acids Research* **38**(19), 6526–6532 (2010).
29. Schaefer, D. W., Joanny, J. F., and Pincus, P., "Dynamics of semiflexible polymers in solution," *Macromolecules* **13**(5), 1280–1289 (1980).
30. Manning, G. S., "The persistence length of {DNA} is reached from the persistence length of its null isomer through an internal electrostatic stretching force," *Biophysical Journal* **91**(10), 3607 – 3616 (2006).
31. Edelstein, A., Amodaj, N., Hoover, K., Vale, R., and Stuurman, N., [*Computer Control of Microscopes Using μManager*], John Wiley & Sons, Inc. (2010).
32. Whitesides, G. M. and Grzybowski, B., "Self-assembly at all scales," *Science* **295**(5564), 2418–21 (2002).
33. Gao, B., Arya, G., and Tao, A. R., "Self-orienting nanocubes for the assembly of plasmonic nanojunctions," *Nature nanotechnology* **7**(7), 433–7 (2012).